Heliyon

ELSEVIER

Received:
21 January 2018
Revised:
19 April 2018
Accepted:
7 June 2018

Cite as: Wanghui Chen, Maxence Wilmet, Thai Giang Truong, Noée Dumait, Stéphane Cordier, Yoshio Matsui, Toru Hara, Toshiaki Takei, Norio Saito, Thi Kim Ngan Nguyen, Takeo Ohsawa, Naoki Ohashi, Tetsuo Uchikoshi, Fabien Grasset. Embedding hexanuclear tantalum bromide cluster $\{Ta_6Br_{12}\}$ into SiO_2 nanoparticles by reverse microemulsion method. Heliyon 4 (2018) e00654. doi: 10.1016/j.heliyon.2018.e00654

Embedding hexanuclear tantalum bromide cluster $\{Ta_6Br_{12}\}$ into SiO_2 nanoparticles by reverse microemulsion method

Wanghui Chen [a,d,*], **Maxence Wilmet** [a,b], **Thai Giang Truong** [b], **Noée Dumait** [b], **Stéphane Cordier** [b], **Yoshio Matsui** [d], **Toru Hara** [e], **Toshiaki Takei** [f], **Norio Saito** [a,d], **Thi Kim Ngan Nguyen** [a,d], **Takeo Ohsawa** [c,d], **Naoki Ohashi** [a,c,d], **Tetsuo Uchikoshi** [a,d], **Fabien Grasset** [a,d,*]

[a] *CNRS-Saint Gobain, UMI 3629, Laboratory for Innovative Key Materials and Structures (LINK), National Institute of Material Science, 1-1 Namiki, Tsukuba, Ibaraki, 305-0044, Japan*

[b] *Univ Rennes, CNRS, ISCR (Institut des Sciences Chimiques de Rennes) – UMR 6226, F-35000 Rennes, France*

[c] *NIMS-Saint-Gobain Center of Excellence for Advanced Materials, National Institute of Material Science, 1-1 Namiki, Tsukuba, Ibaraki, 305-0044, Japan*

[d] *Research Center for Functional Materials (RCFM), National Institute for Materials Science, 1-1 Namiki, Tsukuba, Ibaraki, 305-0044, Japan*

[e] *Research Center for Structural Materials, National Institute for Materials Science, 1-2-1 Sengen, Tsukuba, Ibaraki, 305-0047, Japan*

[f] *Research Network and Facility Services Division, National Institute for Materials Science, 1-1 Namiki, Tsukuba, Ibaraki, 305-0044, Japan*

[*] Corresponding authors.
E-mail addresses: CHEN.Wanghui@nims.go.jp (W. Chen), fabien.grasset@univ-rennes1.fr (F. Grasset).

Abstract

Hexanuclear tantalum bromide cluster units $[\{Ta_6Br^i_{12}\}L^a_6]$ (i = inner, a = apical, L = ligand OH or H_2O) are embedded into SiO_2 nanoparticles by a reverse microemulsion (RM) based method. $[\{Ta_6Br^i_{12}\}Br^a_2\ (H_2O)^a_4]\cdot nH_2O$ (noted TBH) and tetraethyl orthosilicate (TEOS) are used as the starting cluster compound and the precursor of SiO_2, respectively. The RM system in this study consists of the

https://doi.org/10.1016/j.heliyon.2018.e00654

n-heptane (oil phase), Brij L4 (surfactants), ethanol, TEOS, ammonia solution and TBH aqueous sol. The size and morphology of the product namely $\{Ta_6Br_{12}\}$ @SiO_2 nanoparticles are analyzed by HAADF-STEM and EDS mappings. The presence and integrity of $\{Ta_6Br_{12}\}$ in the SiO_2 nanoparticles are evidenced by EDS mapping, ICP-OES/IC and XPS analysis. The optical properties of $\{Ta_6Br_{12}\}$@SiO_2 nanoparticles are analyzed by diffuse reflectance UV-vis spectroscopy, further evidencing the integrity of the embedded $\{Ta_6Br_{12}\}$ and revealing their oxidation state. Both $\{Ta_6Br_{12}\}^{2+}$ and $\{Ta_6Br_{12}\}^{3+}$ are found in SiO_2 nanoparticles, but the latter is much more stable than the former. The by-products in this RM-based synthesis, as well as their related factors, are also discussed.

Keywords: Materials chemistry, Materials science, Nanotechnology

1. Introduction

Over the past several decades, hexanuclear tantalum bromides have attracted considerable attention, in particular as a commercial tool for the phase determination of large biological assemblies by X-ray crystallography and as radiographic contrast agents [1, 2, 3, 4]. More recently, they have been proposed as efficient UV-NIR blockers for the potential application in saving energy window technology [5, 6]. Most hexanuclear tantalum bromides possess the cluster cores of $\{Ta_6Br_{12}\}$, which consists of an octahedral Ta_6 atom cluster and the 12 inner Br ligands bridging over all the 12 Ta-Ta bonds [7]. The oxidation state of $\{Ta_6Br_{12}\}$ can be either 2+, 3+ or 4+, corresponding to 16, 15, and 14 valence electrons involved in its Ta_6 atom clusters, respectively [8, 9]. In most cases, 6 apical positions of Ta_6 atom cluster are further terminated by 6 ligands L (*e.g.*, Br, Cl, H_2O). These ligands are called "apical ligands" to distinguish them from the 12 inner Br ligands of $\{Ta_6Br_{12}\}$. Fig. 1 shows a typical geometry of cluster unit, as the combination of $\{Ta_6Br_{12}\}$ cluster core and its apical ligands, which can be represented as the formula of $[\{Ta_6Br^{i}_{12}\}^{x+}L^{a}_{6}]$ (i = inner, a = apical, x = oxidation state 2, 3, or 4, L = ligand). The preparation of hexanuclear tantalum bromides relies on solid-state reactions performing at high temperature, while the $\{Ta_6Br_{12}\}$ cluster cores in those products are fixed in extended arrays [7, 10]. For instance, reducing $TaBr_5$ by Ta (or other reductant metals) produces Ta_6Br_{15} compounds, where the contained $\{Ta_6Br_{12}\}^{3+}$ cluster cores connect with adjacent ones by sharing their apical Br ligands [7, 11]. $A_4Ta_6Br_{18}$ (A = alkali metal) are prepared by reducing $TaBr_5$ in the presence of ABr_5 [12, 13]. These ternary compounds are built up on the densely packed $[\{Ta_6Br^{i}_{12}\}Br^{a}_{6}]^{4-}$ cluster units (*i. e.*, $\{Ta_6Br_{12}\}^{2+}$ terminated by 6 apical Br ligands), whose charge is counter balanced by alkali metal cations A [9]. Dissolving the solid-state hexanuclear

https://doi.org/10.1016/j.heliyon.2018.e00654

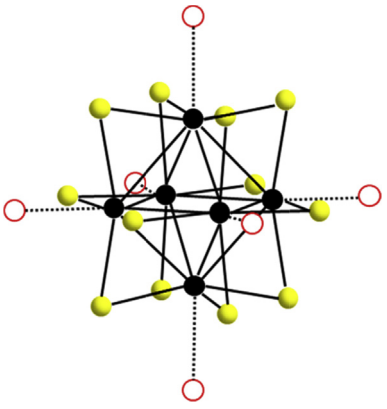

Fig. 1. Structures of an octahedral $\{Ta_6Br_{12}\}$ cluster core terminated by six axial ligands L; the black, yellow, and red spheres represent Ta atoms, edge-bridging Br anions, and terminal-ligands L, respectively.

tantalum bromides products solvated $\{Ta_6Br_{12}\}$ species, as solvent molecules lie in apical positions to form $[\{Ta_6Br^i_{12}\}Br^a_nS^a_{6-n}]^{x-n}$ (S = solvent; $x = 2, 3, 4$; $0 \leq n \leq 6$; $n \neq x$) cluster units [7, 14]. These cluster units are charged and act like ion, and obviously, $\{Ta_6Br_{12}\}$ cluster cores in this case are liberated and attain discrete distribution in solvent [15]. The discrete $\{Ta_6Br_{12}\}$ species are highly interesting because of their ultra-small size (*ca*. 1 nm) and the distinct electronic structure brought by the coexistence of metal-metal and covalent bonds, while they also bear the starting point of various solution based chemical/physical reactions to obtain various kinds of $[\{Ta_6Br^i_{12}\}L^a_6]$ derivatives [7, 10, 16, 17, 18, 19]. Moreover, the electronic structure of discrete $\{Ta_6Br_{12}\}$ species endows their variable optical property, depending on both the oxidation state of $\{Ta_6Br_{12}\}$ (2+, 3+ or 4+) and the properties of apical ligands −thus they can be used as the dye for transparent optical devices [5, 6, 20, 21, 22]. Meanwhile, the ion-like behaviors and ultra-small size of the discrete $\{Ta_6Br_{12}\}$ species can facilitate their homogeneous distribution in matrix and minimize the decreasing on transparency. However, to the best of our knowledge, routine method to embed the discrete $\{Ta_6Br_{12}\}$ species into inorganic matrix has not been established yet.

Reverse microemulsion (RM) is an isotropic and dynamically stable system consisting of oil, water, surfactants and sometimes co-surfactants. The water phase in RM system is well confined to uniform and nanosized swollen micelles (<100 nm), and thus it has been frequently used as the "nanoreactors" for the aqueous mediated reactions. Especially taking the advantage of the uniform size of nanoreactors, monodisperse nanoparticles can be produced in the RM based synthetic process [23, 24, 25]. This process is also efficient to combine two or more kinds of substances into nanocomposite with complex architecture

https://doi.org/10.1016/j.heliyon.2018.e00654

and to embed ultra-small particles into nanosized matrix, though for the latter it seems so far only the synthesis of the SiO_2-based nanocomposites have been well documented [26, 27, 28, 29, 30, 31, 32]. To prepare the so-called functionalized SiO_2 nanoparticles, silicon alkoxide ($Si(OR)_4$) is usually used as the precursor. Accordingly, the pH of the water phase of RM system is adjusted to over 11 to facilitate the hydrolysis and condensation over $Si(OR)_4$ [24]. The substances expected to be embedded into SiO_2 can either be pre-synthesized or be synthesized in situ in RM system. In the former case, the substances which possess hydrophilic surface end up to the nanoreactors after they dispersed in the RM system and are subsequently immobilized on the on-going condensing networks of $\equiv Si-O-Si\equiv$. Even the substances with hydrophobic surface can also be embedded, relying on the "ligand exchanging" process with partially hydrolyzed $Si(OR)_4$ [33, 34]. In the latter case, the reaction become relative more complicated, as considerable attention should be devoted to the compatibility between the formation rates of the nanoparticles and of SiO_2 matrix [28]. To date, several nanocomposites like $Au@SiO_2$, $Ag/Pd@SiO_2$, $CdSe@SiO_2$, $ZnFe_2O_4@SiO_2$, $Fe_3O_4@SiO_2$, $CeO_2@SiO_2$, $MoO_3@SiO_2$, $Ru(bpy)_3^{2+}@SiO_2$, etc. have been successfully prepared [35, 36, 37, 38, 39]. Most recently, the SiO_2-based nanocomposites consisting of Mo_6 and Re_6 clusters have also been successfully prepared [40, 41, 42, 43, 44]. It was demonstrated that these hexanuclear metal halide cluster units can maintain their discrete distribution in SiO_2 nanoparticles and show considerably high stability [41].

Based on the previous works, the present study is proposed to synthesize the SiO_2 nanoparticles functionalized by discrete $\{Ta_6Br_{12}\}$ species (noted $\{Ta_6Br_{12}\}@SiO_2$) by RM based process. The objectives consisted are to find the conditions of a controllable and direct dispersion of a large amount of discrete $\{Ta_6Br_{12}\}$ species into the nanosized SiO_2 matrix. So far, it is the first report on this topic. The advantages of SiO_2 matrix are evidenced for biotechnology and saving energy applications due to a low toxicity, high stability, easy functionalization and high transparency. Although the RM based synthesis for functionalized SiO_2 nanoparticles has been well established, there is a specific challenge to obtain the expected products. Indeed, the pH of the water phase in RM system should be over 11 to grantee the considerable formation rate of SiO_2, but the discrete $\{Ta_6Br_{12}\}$ species show much higher reactivity than other metal cluster species in basic aqueous solution, generating the precipitations of $[\{Ta_6Br_{12}^i\}(OH)_x^a\cdot(H_2O)_{6-x}^a]\cdot nH_2O$ (x = 2, 3, 4) [45]. Even worse, both the hydrolysis and oxidation of $\{Ta_6Br_{12}\}$ will be accelerated in the presence of OH^-, resulting in the breaking down of Ta_6Br_{12} structural edifice and the formation of tantalum oxides. In other words, new substances will possibly generate in the RM system during the formation of SiO_2 matrix. Therefore, the products in this study are carefully characterized to prove the integrity of the encapsulated

https://doi.org/10.1016/j.heliyon.2018.e00654

$\{Ta_6Br_{12}\}$ species, as well as their distribution, oxidation state and optical properties.

2. Experimental

2.1. Materials

Ethanol (99.5%), Ammonia solution (28 wt. %) and tetraethyl orthosilicate (TEOS, 95%) were purchased from Wako Pure Chemical Industries. *n*-heptane (98%) was purchased from Kanto Chemical Co. Nonionic surfactant Brij L4 was purchased from Sigma-Aldrich. DI water was purchased from Yamato Kagaku Co. All the chemicals were used as received without further purification. The starting compound $[\{Ta_6Br^{i}_{12}\}Br^{a}_{2}(H_2O)^{a}_{4}]\cdot nH_2O$ (TBH) was synthesized according to a published procedure [13].

2.2. Methods

n-hepane, Brij L4, ethanol and TEOS were used as received, like oil, surfactant, co-surfactant and the precursor of SiO_2 in this RM based synthesis, respectively. TBH sol was prepared by distributing TBH powder in 1 ml DI water. To ensure its uniformity, TBH sol was first treated by ultrasonication for 15 min and then stirred for 2 hr. In different synthesizes, the concentration of TBH sol (C_{TBH}) was varied from 10 to 50 mM. 3.75 ml Brij L4 and 11.75 ml *n*-heptane were mixed in a flask by vigorous stirring. Green and transparent RM formed immediately after the addition of 0.2 ml TBH solution. The stirring rate was then slowed down to 500 rpm and kept steady until the end of this synthesis. Thereafter, ethanol (volume varied from 0 to 0.6 ml in different synthesizes) and 0.325 ml diluted NH_3 solution (6.5 wt. %) were added in successively with an interval of 5 min. The SiO_2 generation reaction was started by adding 0.1 ml TEOS into the RM system, and then allowed to last for 72 hr. Temperature was controlled steady at 22 °C. After the reaction, the RM system was destabilized by stirring with additional 20 ml ethanol. Dark-green particles settled down soon after the stirring stopped, leaving a colorless upper liquid. After decanting the upper liquid, the particles were collected by centrifugation (11000 rpm, 30 min) and re-dispersed in DI water by ultrasonication treatment. To obtain particles with clean surface, this washing step was repeated for 10 times. Acid washing was applied in case to remove the unexpected impurities, performed with 0.1 mM HCl solution for 3 times. Finally, the collected particles were dried in vacuum at 40 °C for 12 hr.

2.3. Instrumentation

High angle annular dark field scanning transmission electron microscopy (HAADF-STEM) images were acquired by JEM-2100F (JEOL Co.) at 200 kV. The

https://doi.org/10.1016/j.heliyon.2018.e00654

compositional analysis was performed by the energy dispersive X-ray spectrometer (EDS) with double wide detecting area (100 mm^2) detectors equipped in a JEM-2800 (JEOL Co.) operating at 100 kV. To prepare the specimen for HAADF-STEM and EDS analysis, a small amount of RM containing the resulting $\{Ta_6Br_{12}\}@SiO_2$ nanoparticles was placed on an elastic carbon film covered Cu grid. To remove the excessive surfactants, this Cu grid was washed with dichloromethane after dry. The specimen of washed $\{Ta_6Br_{12}\}@SiO_2$ nanoparticles was prepared by placing a small amount of its water suspension on carbon film covered Cu grid, which had been treated by plasma, and completely dried in ambient condition. Powder X-ray diffraction (XRD) patterns were acquired by a D/MAX Ultima III (Rigaku Co.) diffractometer using Cu Kα radiation ($\lambda = 1.5418$ Å) over a range of $5° < 2\theta < 60°$. The X-ray photoelectron spectra (XPS) were recorded using a SigmaProbe (Thermos Fisher Co.) spectrometer, with using Al-Kα line (1486.6 eV) as the excitation source. XPS data treatments were carried out using the software ThermoAvantage and the spectra energy was calibrated with the first deconvolved C1s peak (attributed to the C−C bonding) rescaled at 284.8 eV. IR spectra were collected in the 4000-400 cm^{-1} range by a Nicolet TM 4700 FTIR spectrometer (Thermos Fisher Co.), by using KBr sampling technique. Diffuse reflectance UV-vis-NIR spectra were collected by an integrating sphere equipped V-7200 spectrometer (Jasco Co.). The absorbance UV-vis-NIR spectra of discrete $\{Ta_6Br_{12}\}^{2+}$ and $\{Ta_6Br_{12}\}^{3+}$ species were also collected with the sol of TBH in water and NaOH solution (molar ratio of $OH^-/Ta_6 = 8$), respectively [45]. To confirm the molar ratio of Ta/Si and Br/Si in the resulting $\{Ta_6Br_{12}\}@SiO_2$ nanoparticles, ICP-OES (for Ta and Si) and ion chromatography (IC, for Br) analysis were performed.

3. Results

3.1. Phenomenology

Each $\{Ta_6Br_{12}\}$ in the starting TBH is in the oxidation state of 2+ and terminated by 2 Br and 4 H_2O ligands, while the formed neutral cluster units $[\{Ta_6Br^i_{12}\}Br^a_2(H_2O)^a_4]$ densely packed with a certain amount of water molecules to form crystal structure [13, 46]. As seen in Fig. 2, TBH fully dissolved in water and formed a homogeneous sol, whose characteristic emerald-green color implies the formation of $[\{Ta_6Br^i_{12}\}(H_2O)^a_6]^{2+}$ cluster units [45]. The RM system composed of the TBH sol, Brij L4, *n*-heptane and ethanol were obtained subsequently, showing high homogeneity and transparency, as well as maintaining the emerald-green color. Due to the change of pH, this RM system immediately became dark green after the addition of ammonia solution. The addition of ammonia solution could also lead to turbidity, reflecting the generation of precipitates, while the rate and degree of turbidity strongly depended on the concentration of TBH sol (C_{TBH}). For instance, the RM system maintained high transparency when $C_{TBH} = 10$ mM, whereas it

https://doi.org/10.1016/j.heliyon.2018.e00654

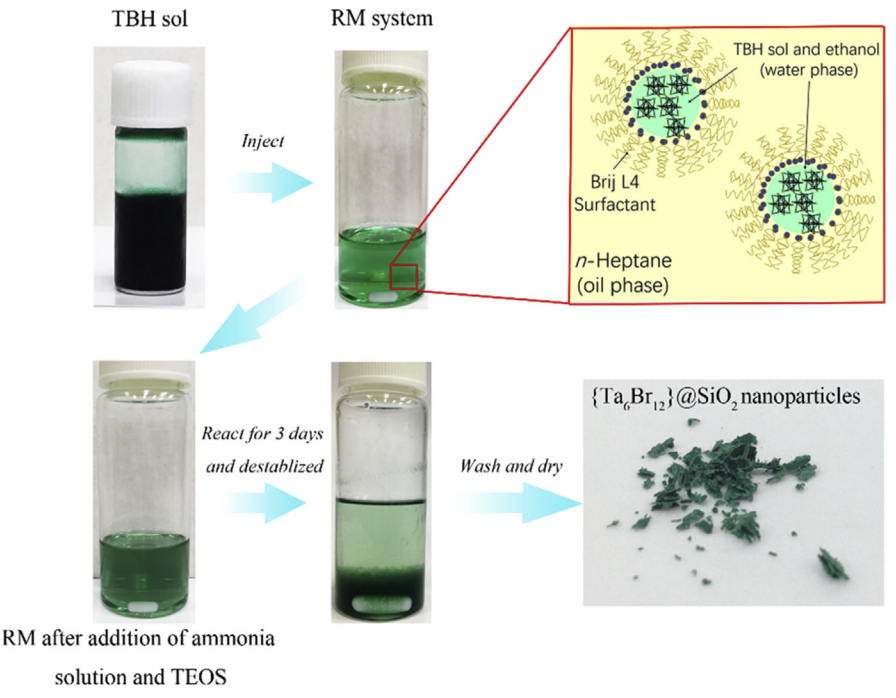

Fig. 2. Digital photographs of the RM system in different stages of the synthesis and the finally produced $\{Ta_6Br_{12}\}@SiO_2$ nanoparticles.

became turbid in *ca.* 5 min if C_{TBH} increased to 30 mM. After a sufficient reaction time for SiO_2 formation (3 days), this RM system was destabilized by stirring with excessive ethanol. Dark green particles settled down as soon as the stirring stopped, leaving colorless supernatant. After washing and drying steps, dark-green powder was obtained as the final product.

3.2. Morphology and size

Fig. 3a shows typical HAADF-STEM images of the unwashed$\{Ta_6Br_{12}\}@SiO_2$ nanoparticles. Thanks to the well confined water phase, the formed SiO_2 matrix was controlled to *ca.* 50 nm in size and showed uniform spherical shape. Both the embedded and nonembedded tantalum compounds can be found—the former consists an aggregate core centered in each $\{Ta_6Br_{12}\}@SiO_2$ nanoparticles (blue sphere in Fig. 3b) and also the discrete ultra-small (*ca.* 1 nm) particles in SiO_2 matrix (red spheres in Fig. 3b), the latter consists of the ultra-small particles agglomerating on the outer surface of SiO_2. Fig. 3b indicates the nonembedded tantalum compounds were mostly removed in the washing steps, leaving a clean surface of SiO_2 matrix, while the embedded tantalum compounds seem not to be affected by washing, like that for Mo_6 clusters in the previous study [41]. Fig. 4 shows the HAADF-STEM image of the washed $\{Ta_6Br_{12}\}@SiO_2$ nanoparticles and its corresponding EDS analysis. All the peaks of Si, O, Ta and Br are shown on the EDS spectrum

https://doi.org/10.1016/j.heliyon.2018.e00654

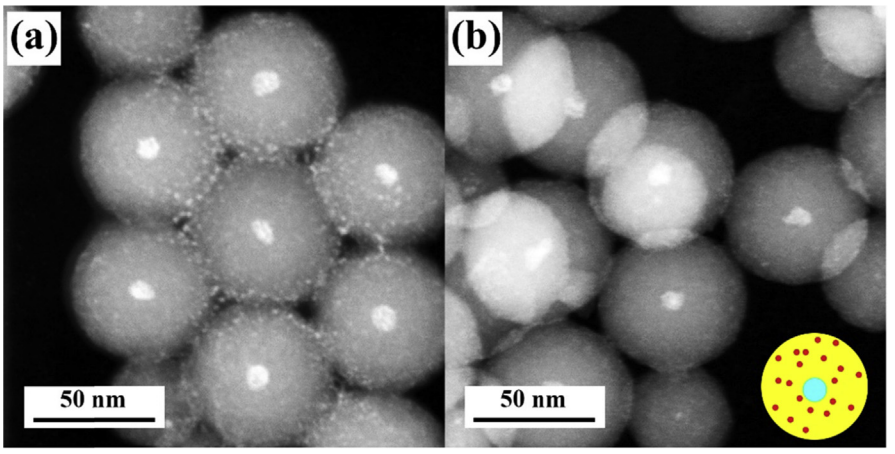

Fig. 3. HAADF-STEM images of $\{Ta_6Br_{12}\}$@SiO_2 nanoparticles (C_{TBH} = 10 mM) sampled before (a) and after (b) washing step; The insert of (a) is the corresponding low magnification HAADF-STEM image, wherein the scale bar represents 200 nm; The insert of (b) demonstrates the architecture of the particles in (b), where the SiO_2 matrix, aggregate core and discrete ultra-small particles are differentiated by yellow, blue and red color, respectively.

(Fig. 4e), indicating tantalum bromides were successfully embedded into the SiO_2 nanoparticles, though it is still hard to confirm at this stage if the embedded tantalum bromides are $\{Ta_6Br_{12}\}$ species. The EDS mappings of Si, Ta and Br elements (Fig. 4b—d) are in good agreement with the morphology shown in Fig. 3b—the embedded tantalum compounds are not only rich in the aggregate core part of SiO_2 nanoparticles but also disperse thoroughly in the whole SiO_2 matrix.

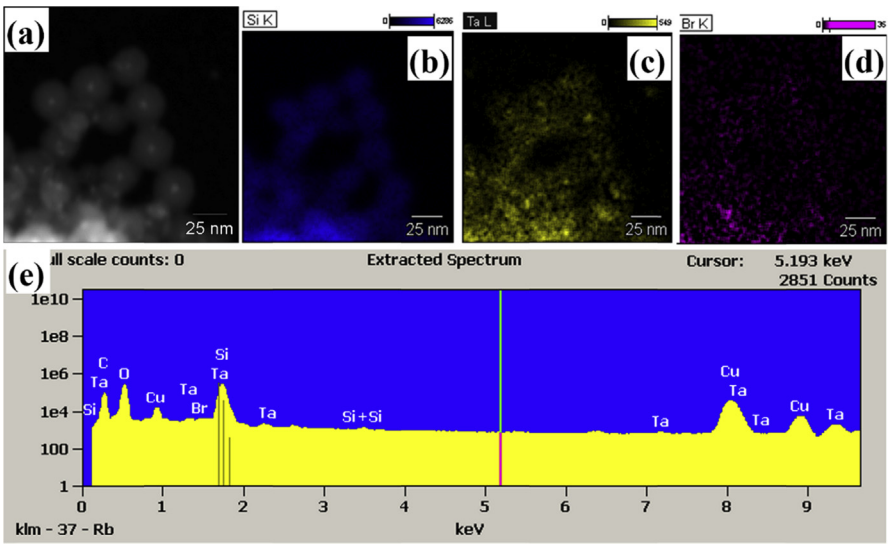

Fig. 4. HAADF-STEM image (a) of $\{Ta_6Br_{12}\}$@SiO_2 nanoparticles (C_{TBH} = 10 mM) and the corresponding EDS mappings indicating the distribution of Si (b) Ta (c), and Br (d) elements; (e) is the EDS spectrum of the full scale of (a).

https://doi.org/10.1016/j.heliyon.2018.e00654

Indicated by a series of syntheses, the amount of the embedded tantalum compounds in SiO_2 matrix strongly depended on C_{TBH} and the molar ratio of ethanol versus H_2O (noted R) in RM system. Fig. 5 shows HAADF-STEM images of the washed $\{Ta_6Br_{12}\}@SiO_2$ nanoparticles synthesized with C_{TBH} = 10, 20, 30, and 40 mM and keeping all other synthetic parameters the same. Particles in all these samples show narrow size distribution due to the advantages of RM system, despite their average size slightly decreases from 50 nm to 40 nm with increasing C_{TBH}. Moreover, increasing C_{TBH} did not vary the size of aggregate core (*ca.* 10 nm) in each particle but significantly increased the density of the ultra-small tantalum compounds in SiO_2 matrix. It is also noteworthy that the nonembedded tantalum compounds started to appear outside of SiO_2 matrix when C_{TBH} reached 40 mM (Fig. 5d). On the other hand, decreasing R in RM system was not favorable for obtaining $\{Ta_6Br_{12}\}@SiO_2$ nanoparticles with homogeneous morphology, because it

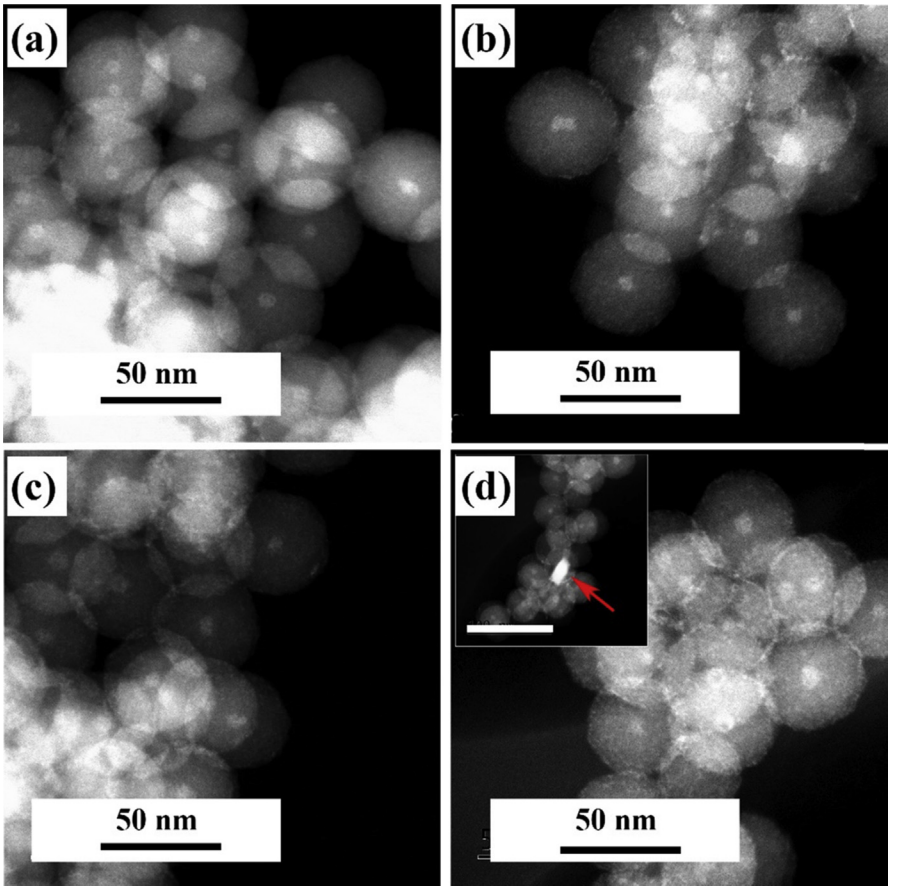

Fig. 5. HAADF-STEM images of the $\{Ta_6Br_{12}\}@SiO_2$ nanoparticles synthesized with C_{TBH} = 10 mM (a), 20 mM (b), 30 mM (c) and 40 mM (d), respectively; all these samples were synthesized with R = 0.37 and washed for 10 times with water; the insert of (d) is the corresponding low magnification HAADF-STEM image with an arrow pointing to an irregular shaped aggregate of tantalum compounds out of SiO_2 matrix, wherein the scale bar represents 100 nm.

https://doi.org/10.1016/j.heliyon.2018.e00654

led to the presence of more aggregates of tantalum compounds outside the SiO_2 matrix. As seen in Fig. 6a, when R reduced to 0.24, a number of nonembedded aggregates started to appear outside of SiO_2 matrix despite the low C_{TBH} (30 mM). More representatively, when R = 0 (*i.e.*, no ethanol contained in RM system), the generated nonembedded aggregates were so large that capped on several $\{Ta_6Br_{12}\}$ @SiO_2 nanoparticles (Fig. 6b). Accordingly, only a small number of tantalum compounds were embedded into the SiO_2 nanoparticles (insert of Fig. 6b). In addition, the EDS spectra in Fig. 7 demonstrates both the Ta and Br elements are contained in the irregular shaped aggregates.

3.3. X-ray diffraction analyses

Fig. 8 shows the XRD patterns of the starting TBH and the as-synthesized $\{Ta_6Br_{12}\}$ @SiO_2 nanoparticles synthesized under different conditions. The XRD pattern of TBH (Fig. 8a) agrees with the pattern of $Ta_6Br_{14}\cdot 8H_2O$ reported by Spreckelmeyer et al, reflecting the dense packing of $[\{Ta_6Br^{i}_{12}\}Br^{a}_{2}(H_2O)^{a}_{4}]$ cluster units [47]. Such long-range-order structure is supposed to disappear within the dissolution of TBH and the following RM based process. As expected, no diffraction peak showing on the patterns of $\{Ta_6Br_{12}\}$@SiO_2 nanoparticles can be assigned to the characteristic peaks of TBH. On the patterns of $\{Ta_6Br_{12}\}$@SiO_2 nanoparticles synthesized with C_{TBH} = 10, 20, 30 mM (Fig. 8b–d), the broad peak maximum at $2\theta = 24^{\circ}$ is the most significant, which can be assigned to the amorphous SiO_2 matrix. Despite the sharp diffraction peak maximum at $2\theta = 18^{\circ}$ can hardly be defined at the current stage, it implies the formation of either new densely packed array of cluster units or other tantalum compounds in the $\{Ta_6Br_{12}\}$@SiO_2 nanoparticles. Further take

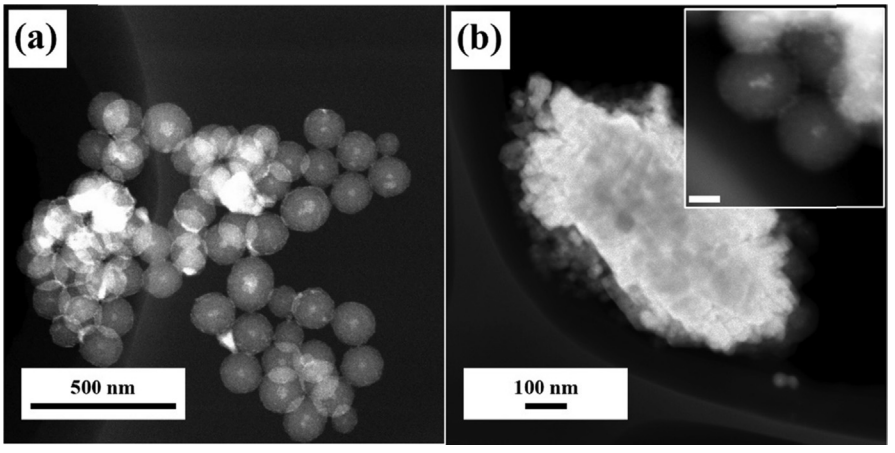

Fig. 6. HAADF-STEM images of $\{Ta_6Br_{12}\}$@SiO_2 nanoparticles synthesized with R = 0.24 (a) and 0 (b); the insert of (b) is the corresponding high magnification image with the scale bar representing 10 nm; both of these two samples were synthesized with C_{TBH} = 30 mM and washed for 10 times with water.

https://doi.org/10.1016/j.heliyon.2018.e00654

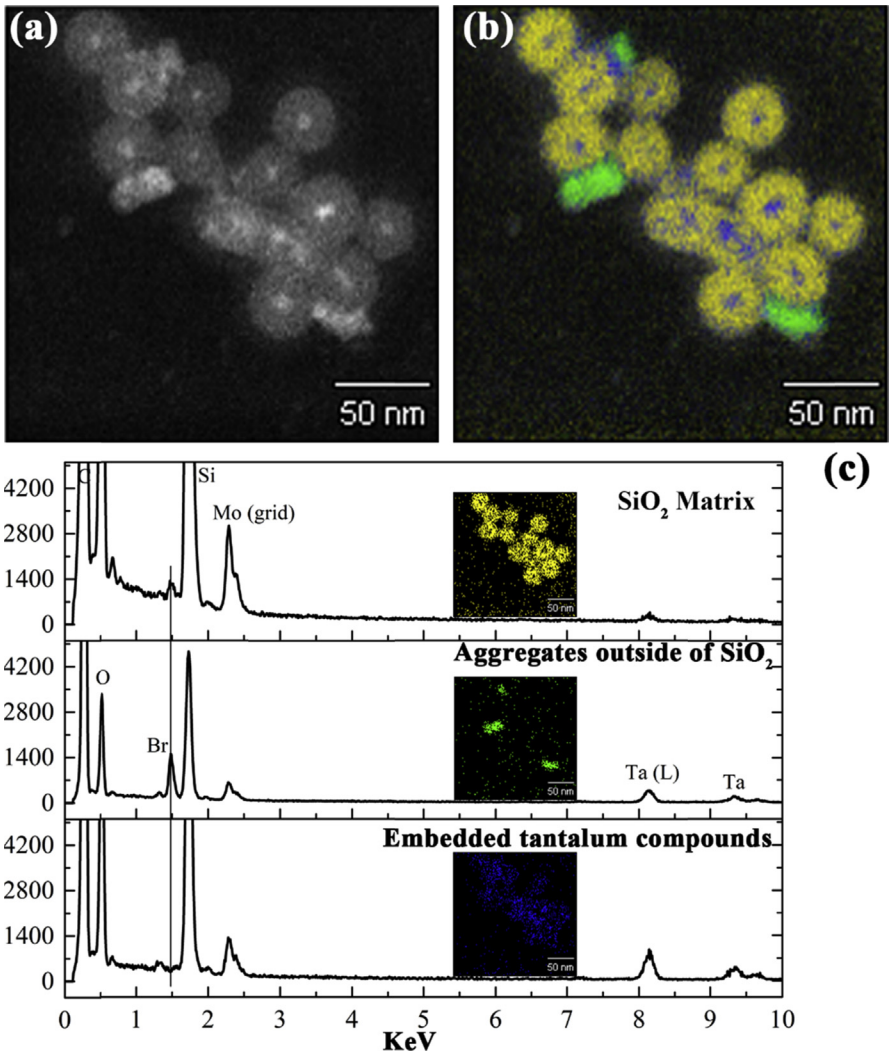

Fig. 7. HAADF-STEM image (a) and the phase mapping from the multi-variant analysis of EDS (b) of the $\{Ta_6Br_{12}\}$@SiO_2 nanoparticles synthesized with C_{TBH} = 40 mM, R = 0.37; (c) show the EDS spectrum of each phase.

account of the texture of these samples (Fig. 5a–c), the tantalum compounds acting as the aggregate cores centered in SiO_2 nanoparticles should be in crystal form, assuming that discrete $\{Ta_6Br_{12}\}$ species are not able to produce diffraction peaks because of the lack of dense packing which leads to crystal structure. Much more diffraction peaks appear on the XRD patterns when C_{TBH} increased to 40 mM (Fig. 8d) or R decreased to 0 (Fig. 8e). Obviously, these peaks can be ascribed to the promptly generated nonembedded aggregates of tantalum compounds, which presented outside of SiO_2 matrix and remained in samples after washing steps. The XRD pattern in Fig. 9 indicates the aggregates were efficiently, though not completely, removed in the acid washing steps.

https://doi.org/10.1016/j.heliyon.2018.e00654

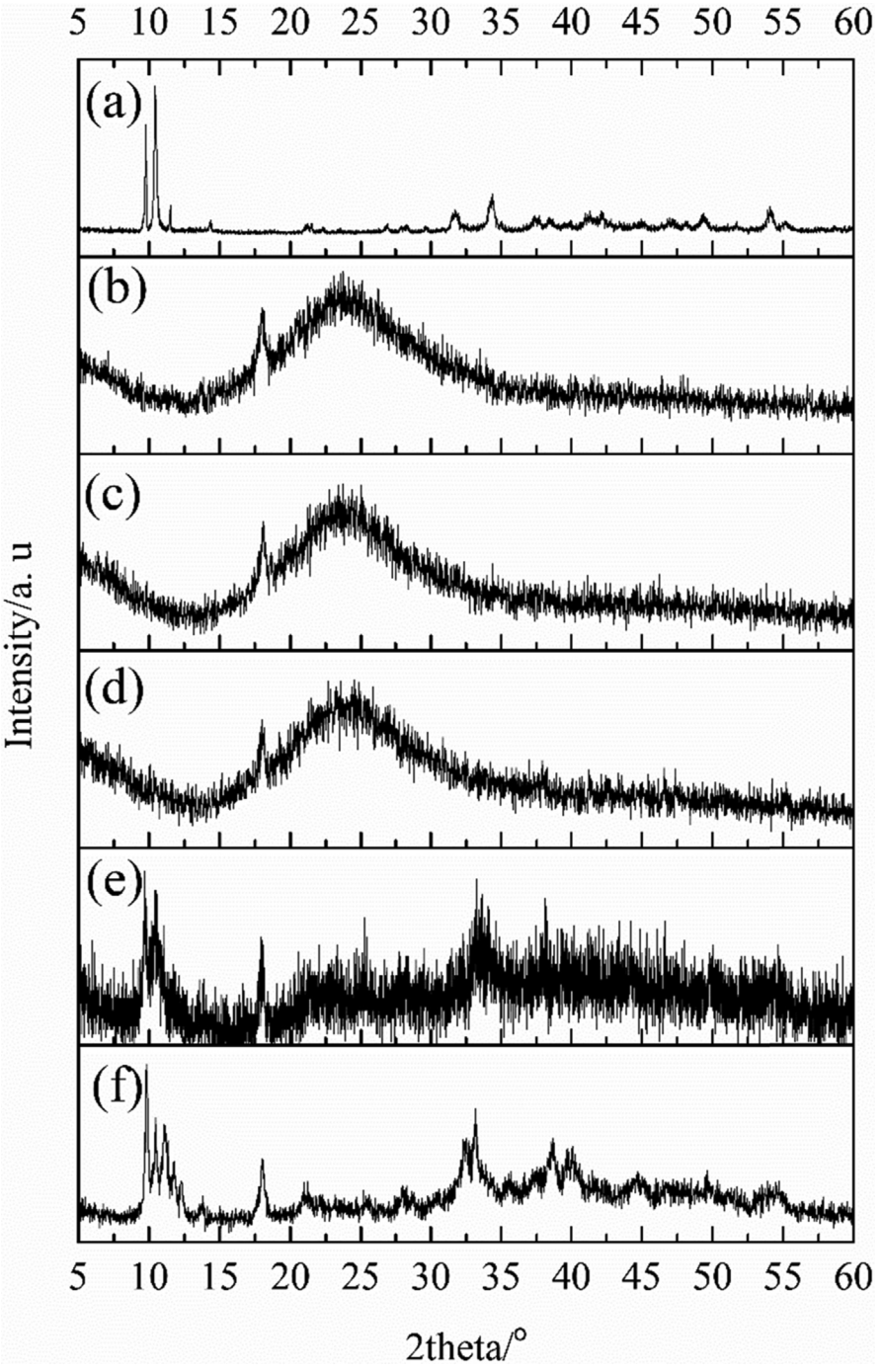

Fig. 8. XRD patterns of the starting TBH (a), $\{Ta_6Br_{12}\}@SiO_2$ nanoparticles synthesized with $C_{TBH} = 10$, $R = 0.37$ (b), $C_{TBH} = 20$, $R = 0.37$ (c), $C_{TBH} = 30$, $R = 0.37$ (d), $C_{TBH} = 40$, $R = 0.37$ (e), and $C_{TBH} = 30$, $R = 0$ (f); all these samples were washed for 10 times with water.

https://doi.org/10.1016/j.heliyon.2018.e00654

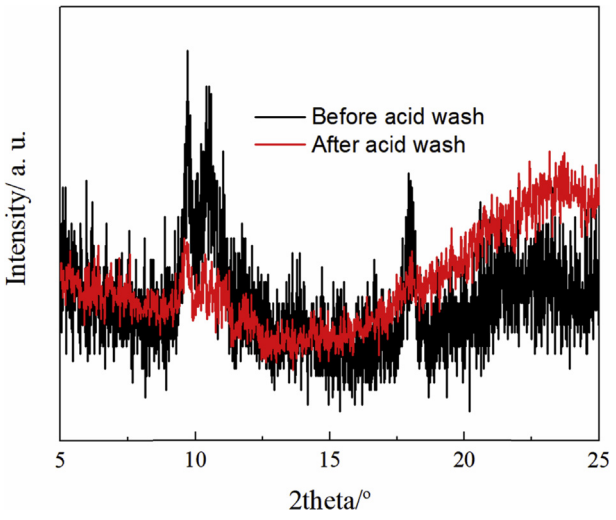

Fig. 9. XRD patterns of the $\{Ta_6Br_{12}\}@SiO_2$ nanoparticles before and after acid wash; these particles were synthesized with $C_{TBH} = 40$ mM, $R = 0$.

3.4. Chemical analysis

A series of ICP-OES/IC characterizations was carried out to determine the actual molar ratio of Ta/Si, Br/Si and Br/Ta in the as-synthesized $\{Ta_6Br_{12}\}@SiO_2$ nanoparticles. For all the washed and acid-washed samples, the molar ratio of Ta/Si and Br/Si were estimated and plotted versus C_{TBH} in Fig. 10a. The corresponding theoretical ratio Ta/Si and Br/Si in each sample was calculated by assuming that all the TEOS has condensed to form SiO_2 and that all the introduced $\{Ta_6Br_{12}\}$ species have been embedded in. Same as that observed for the embedding of Mo_6 metal clusters in SiO_2 nanoparticles, the result show that the amount of embedded tantalum compounds is always below its corresponding theoretical one [41]. Also shown in Fig. 10a, the deviation between the experimental and theoretical values of Ta/Si

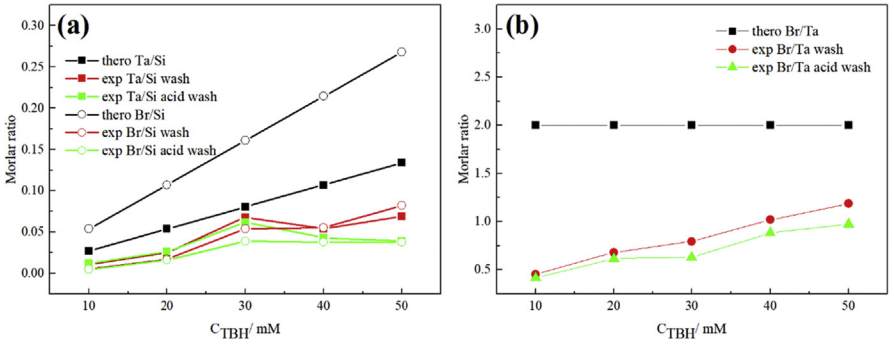

Fig. 10. (a) molar ratios of Ta/Si (full symbols) and Br/Si (empty symbols) obtained by theoretical calculations (black), ICP-OES/IC measurements of water washed (red) and 0.1 mM HCl washed (green) $\{Ta_6Br_{12}\}@SiO_2$ nanoparticles, depending on the C_{TBH}; the molar ratio of Br/Ta in each sample is calculated and plotted versus C_{TBH} in (b).

https://doi.org/10.1016/j.heliyon.2018.e00654

and Br/Si increase as increasing C_{TBH} or after acid-washing process. This observation indicates that the efficiency of the encapsulation of the tantalum compounds inside the SiO_2 nanoparticles is limited by their solubility in the SiO_2. As seen, the molar ratio of Ta/Si increases when $C_{TBH} < 30$ mM and there is no significant difference between the washed and acid-washed samples in this range of C_{TBH}. On contrary when $C_{TBH} > 30$ mM, the molar ratios seem to reach a plateau and there is no increasing of the Ta/Si along with increasing C_{TBH}. Meanwhile, the Ta/Si ratios of the acid-washed samples are much lower than their corresponding washed sample. Such difference is possibly due to the removing of nonembedded clusters in washing step. The trend of Br/Si ratio is close to that of Ta/Si, except the large difference between that of the washed and acid-washed sample starts to appear when $C_{TBH} = 30$ mM. Moreover, the ratio of Br/Ta in each sample, which is also plotted versus C_{TBH} in Fig. 10b, reflects the apparent chemical composition of the embedded tantalum compounds. The theoretical value of 2 for the Br/Ta molar ratio is confirmed as all the embedded tantalum compounds are $[\{Ta_6Br^i_{12}\}L^a_6]$ (L = H_2O or OH), and all the free Br^- in SiO_2 matrix (*i. e.*, the dissociated apical Br ligands, generated within the dissolution of TBH) have been removed in the washing steps. Unfortunately, the Br/Ta ratios in all these samples were much lower than 2, though it increased with increasing of C_{TBH}. This result suggests a considerable portion of $\{Ta_6Br_{12}\}$ species lost their integrity in the embedding process, followed by the removing of the generated free Br^- anions from SiO_2 nanoparticles (in washing steps).

To further study the chemical composition of the embedded tantalum compounds, the Br environment in the $\{Ta_6Br_{12}\}@SiO_2$ nanoparticles was analyzed by XPS characterization. Fig. 11 and Table 1 summarize the acquired Br 3p core-level spectra and peak binding energies, respectively, of both the starting TBH and $\{Ta_6Br_{12}\}@SiO_2$ nanoparticles. As seen, both Br 3p spectra of these two samples are found in the region of 178−194 eV, splitting to two lines of Br $3p_{1/2}$ and Br $3p_{3/2}$. Deconvoluting the Br $3p_{1/2}$ and Br $3p_{3/2}$ energies of TBH gave two sets of spin-orbit doublets (marked by blue and green in Fig. 11a), reflecting the presence of two Br environments in TBH, noted Br_1 and Br_2 in Table 1, respectively. The area ratio of the higher energy to the lower energy doublet (*i.e.*, [Br_1 ($3p_{1/2}$) + Br_1 ($3p_{3/2}$)]: [Br_2 ($3p_{1/2}$) + Br_2 ($3p_{3/2}$)]) was calculated to 6:1. Taking account of the composition of TBH, the higher energy doublet (Br_1) could be assigned to the edge-bridging Br anions, while the lower energy doublet (Br_2) could be assigned to the apical Br ligands. These assignments are consistent with the previous study carried out by Best et al, where the environments of Br_1 and Br_2 were unconventionally denoted as Br_b and Br_t, respectively [48]. Regarding the Br 3p spectrum of $\{Ta_6Br_{12}\}@SiO_2$ nanoparticles, it was also deconvoluted to two sets of doublets (Fig. 11b). Table 1 reveals the higher energy doublet of $\{Ta_6Br_{12}\}@SiO_2$ nanoparticles was in good agreement with that of TBH, in terms of both binding energy and

https://doi.org/10.1016/j.heliyon.2018.e00654

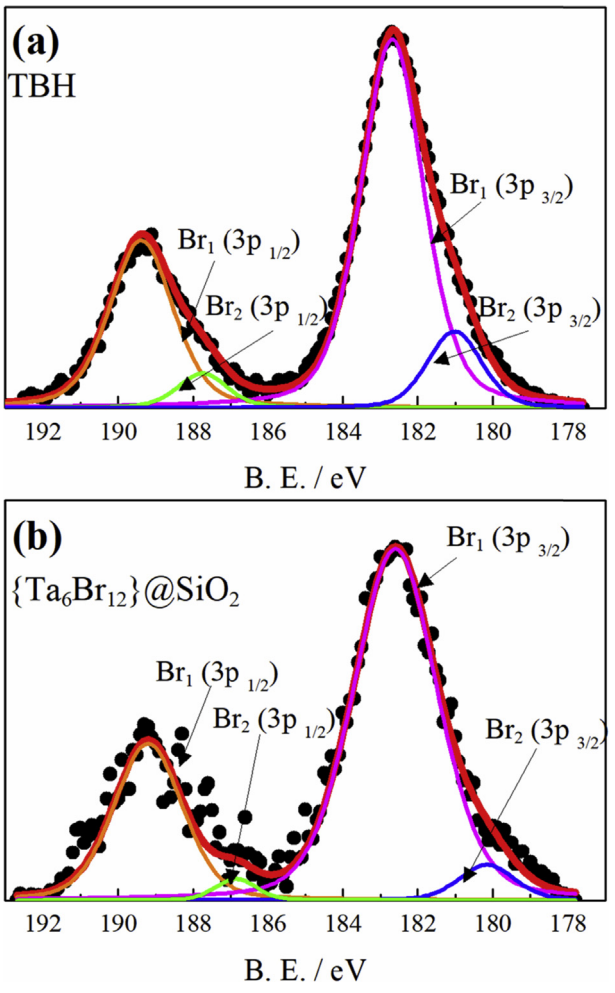

Fig. 11. Br 3p binding energy spectra of TBH (a) and $\{Ta_6Br_{12}\}@SiO_2$ nanoparticles (b); the experimental and fitting curves are plotted in black and red, respectively; the two sets of Br $3p_{1/2,\ 3/2}$ doublet that from deconvolution are differentiated by blue and green colors.

full width at half maximum (FWHM). Therefore, the consistence of the Br_1 environment in the starting TBH and $\{Ta_6Br_{12}\}@SiO_2$ nanoparticles was evidenced, and thus demonstrating the integrity of Ta_6Br_{12} structural edifice maintained in the as-synthesized $\{Ta_6Br_{12}\}@SiO_2$ nanoparticles. It should be point out that this conclusion can only apply to the embedded tantalum compounds near the out surface of SiO_2 matrix, as the tantalum compound in the aggregate core part of $\{Ta_6Br_{12}\}@SiO_2$ nanoparticles is ca. 20 nm far from the out surface but the analysis depth of the current Al-Kα XPS characterizations is ca. 5 nm. On another hand, the lower energy doublet (Br_2) of $\{Ta_6Br_{12}\}@SiO_2$ nanoparticles shows a significant red shift with respect to that of TBH, and the area ratio of Br_1: Br_2 drastically increased to 14:1 (or 12:0.85). Hence, the Br_2 environment of $\{Ta_6Br_{12}\}@SiO_2$ nanoparticles could not be seen as from the apical Br ligands any longer, and is possibly based on the free Br- anions remaining in SiO_2 matrix after the washing steps.

https://doi.org/10.1016/j.heliyon.2018.e00654

Table 1. X-ray photoelectron spectra of Br 3p[a)] in TBH and $\{Ta_6Br_{12}\}@SiO_2$ nanoparticles.

Sample	Br_1[b)]		Br_2[c)]	
	$3p_{1/2}$	$3p_{3/2}$	$3p_{1/2}$	$3p_{3/2}$
TBH	189.4 (2.0)	182.7 (2.0)	187.8 (1.6)	181.0 (1.7)
$\{Ta_6Br_{12}\}@SiO_2$	189.2 (1.9)	182.6 (2.2)	186.8 (1.8)	180.1 (1.9)

[a)] Binding energies in eV, with FWHM values given in parentheses.
[b)] Br_1 represents the Br $3p_{1/2,\ 3/2}$ doublets with higher binding energy.
[c)] Br_2 represents the Br $3p_{1/2,\ 3/2}$ doublets with lower binding energy.

3.5. Optical properties

Fig. 12a plots the diffuse reflectance UV-vis spectra of $\{Ta_6Br_{12}\}@SiO_2$ nanoparticles synthesized with different C_{TBH} (spectrum a-e), and the absorption spectra of discrete $\{Ta_6Br_{12}\}^{2+}$ and $\{Ta_6Br_{12}\}^{3+}$ species in aqueous solution are shown in

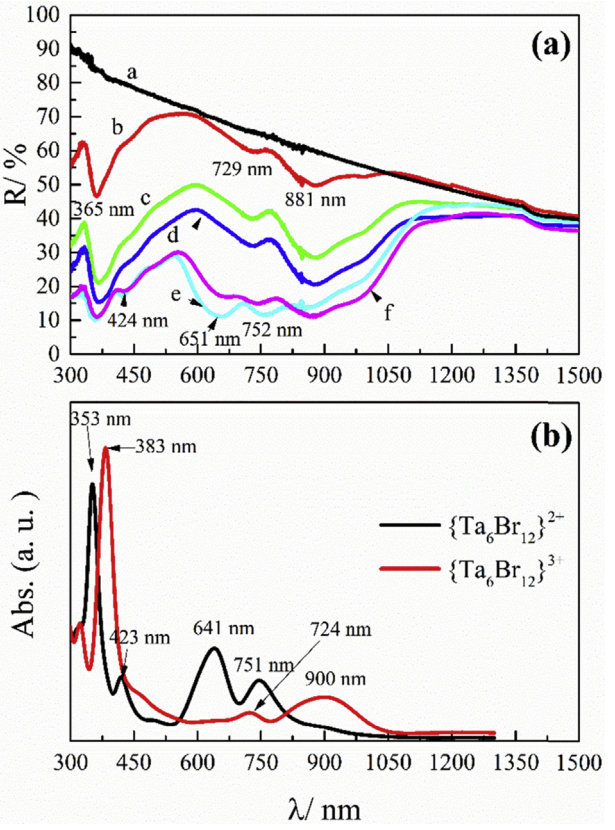

Fig. 12. (a) the diffuse reflectance UV-vis-NIR spectra of the $\{Ta_6Br_{12}\}@SiO_2$ nanoparticles synthesized with $C_{TBH} = 0$ mM (spectrum a), 10 mM (spectrum b), 20 mM (spectrum c), 30 mM (spectrum d) and 40 mM (spectrum e); spectrum f corresponds to the sample synthesized with $C_{TBH} = 40$ mM and aged for 2 months; (b) the UV-vis absorption spectra of aqueous solution containing discrete $\{Ta_6Br_{12}\}^{2+}$ and $\{Ta_6Br_{12}\}^{3+}$ species.

https://doi.org/10.1016/j.heliyon.2018.e00654

Fig. 12b for reference. To eliminate the effect of the impurity of tantalum compound aggregates formed outside SiO_2 nanoparticles on the spectrum, the $\{Ta_6Br_{12}\}$@SiO_2 nanoparticles synthesized with $C_{TBH} = 40$ mM were pretreated with 0.1 mM HCl solution. As seen, there is no significant absorption peak appears on the reflectance spectrum of pure SiO_2 nanoparticles (*i.e.*, synthesized with $C_{TBH} = 0$, spectrum a) within the wavelength range from 300 to 1500 nm. Functionalizing these SiO_2 nanoparticles with discrete $\{Ta_6Br_{12}\}$ species ($C_{TBH} \leq 30$ mM, spectrum b, c, and d) introduced several absorption bands in UV-vis-NIR region, which were maximum at the wave length of 365, 729, and 881 nm respectively. The intensities of absorption bands increased with increasing C_{TBH}, keeping their position consistent with each other. Moreover, all the absorption peaks of these $\{Ta_6Br_{12}\}$@SiO_2 nanoparticles show one to one correspondence with those of discrete $\{Ta_6Br_{12}\}^{3+}$ species in aqueous solution, maximum at the wavelength of 383, 724 and 900 nm. Despite the slight shifts between the absorption of $\{Ta_6Br_{12}\}$ species in SiO_2 matrix and that of $\{Ta_6Br_{12}\}^{3+}$ species in aqueous solution, this correspondence indicates the 3+ oxidation state of the embedded $\{Ta_6Br_{12}\}$ [7, 8, 20, 21, 22, 49]. The $\{Ta_6Br_{12}\}^{2+}$ only presented in the $\{Ta_6Br_{12}\}$@SiO_2 nanoparticles synthesized with $C_{TBH} = 40$ mM (spectrum e), indicated by three new absorptions maximum at the wavelength of 424, 651, and 752 nm, which show one to one correspondence with the characteristic absorption of $\{Ta_6Br_{12}\}^{2+}$ species in aqueous solution (maximum at the wavelength of 423, 641 and 751 nm). However, the spectrum f in Fig. 12a, corresponding to the $\{Ta_6Br_{12}\}$@SiO_2 nanoparticles synthesized with $C_{TBH} = 40$ mM and had been stored for 2 months, suggests the discrete $\{Ta_6Br_{12}\}^{2+}$ species in SiO_2 matrix were much more unstable, as all the characteristic absorptions of $\{Ta_6Br_{12}\}^{2+}$ species decreased along with the increasing absorption at the wavelength of 881 nm.

4. Discussion

Two reactions took place in the RM based process: i) the reaction of $[\{Ta_6Br^i_{12}\}(H_2O)^a_6]^{2+}$ cluster units with NH_4OH and ii) the formation of SiO_2 nanoparticles. Unlike the well documented latter one, the former reaction can be considerably complicated. According to previous studies on the base titration of $[\{Ta_6Br^i_{12}\}(H_2O)^a_6]^{2+}$ cluster units in aqueous solution, the reactions of precipitation (generating $[\{Ta_6Br^i_{12}\}(OH)^a_x(H_2O)^a_{6-x}]\cdot nH_2O$ (x = 2, 3, 4), oxidation (generating $\{Ta_6Br_{12}\}^{3/4+}$ species) and decomposition of Ta_6Br_{12} structural edifice (generating $TaBr_xO_y$ compound) may take place [45]. Therefore, the distribution, oxidation state and integrity of the embedded $\{Ta_6Br_{12}\}$ species in SiO_2 matrix should be carefully discussed. Indeed, we observed four tantalum compound related phases by HAADF-STEM analysis, as the (1) ultra-small particles in SiO_2 shells, (2) aggregate cores centered in SiO_2 nanoparticles, (3) ultra-small particles adhering on the surface of SiO_2 shells, and (4) irregular shaped aggregates outside of SiO_2 matrix.

https://doi.org/10.1016/j.heliyon.2018.e00654

According to the previous characterizations, properties of phase (1) can be summarized as i) consisting of the discretely dispersed tantalum compounds, the size of which is comparable with that of a single cluster (by HAADF-STEM and EDS mapping characterizations); ii) maintaining the integrity of Ta_6Br_{12} structural edifice (by XPS characterization); iii) introducing concentrated phase (1) by using high C_{TBH} leads to the increased absorptions of $\{Ta_6Br_{12}\}@SiO_2$ (by diffuse reflectance UV-vis-NIR characterizations). Therefore, we can demonstrate that the phase (1) consists of discrete $\{Ta_6Br_{12}\}$ species embedded in SiO_2 matrix, which is also the objective product of this study. The diffuse reflectance UV-vis spectra also demonstrated that most all the embedded $\{Ta_6Br_{12}\}$ are in the oxidation state of 3+, while the $\{Ta_6Br_{12}\}^{2+}$ could be found in the samples synthesized with high C_{TBH} but showing poor stability even in ambient condition. The transformation from $\{Ta_6Br_{12}\}^{2+}$ species (in TBH and its sol) to $\{Ta_6Br_{12}\}^{3+}$ species (in $\{Ta_6Br_{12}\}@SiO_2$ nanoparticles) was possibly due to the accelerated oxidation rate of $[\{Ta_6Br^{i}_{12}\}(H_2O)^{a}_{6}]^{2+}$ cluster units in basic solution. Though this process can hardly be prevented at current stage of this study, the obtained SiO_2 nanoparticles functionalized by $\{Ta_6Br_{12}\}^{3+}$ species are still very interesting for UV-NIR blockers or other optical applications, attributed to their strong absorptions in both the UV and NIR regions [5, 6]. Furthermore, the apical ligands of the $\{Ta_6Br_{12}\}$ in phase (1) can be either H_2O or OH^- but not Br^-, as the XPS characterization revealed the apical Br dissociated within the RM based process. It is also indicated the free Br^- anions were removed to a considerable extent in washing steps, resulted in the high Br_1: Br_2 (12: 0.85). Therefore, by assuming the residues of Br^- in SiO_2 matrix acting as the counter anions, the structure of cluster units in phase (1) can be written as $Br_{0.85}[\{Ta_6Br^{i}_{12}\}^{3+}(H_2O)^{a}_{3.85}(OH)^{a}_{2.15}]$. In case of the $\{Ta_6Br_{12}\}^{2+}$ species, these cluster units can be written as $Br_{0.85}[\{Ta_6Br^{i}_{12}\}^{2+}(H_2O)^{a}_{4.85}(OH)^{a}_{1.15}]$. Aubert et al proposed a similar formula for the embedded Mo_6 species in SiO_2 matrix, which could be used to explain the strong interaction between cluster units matrix— hydrogen bonds formed between the apical ligands OH^- and Si-OH groups [41].

The embedded tantalum compounds also contain the phase (2)—consisting of an aggregate core in the center of each SiO_2 nanoparticle. However, these compounds cannot be seen as consisting of discrete cluster units any more, as they show a much larger size (*ca.* 10 nm) and XRD analysis suggested they possess crystal structure. Though EDS mapping indicated these cores composed by Ta and Br elements, but it is still hard to know their actual composition. The ICP-OES/IC results indicated the apparent molar ratio of Br/Ta of all the embedded tantalum compounds is lower than theoretical 2, indicating the decomposition of a proportion of $\{Ta_6Br_{12}\}$. Because phase (1) has been proved to the discrete cluster units with the molar ratio of Br/Ta slightly larger than 2, the breaking down of the Ta_6Br_{12} structural edifice possibly took place within the formation of aggregate cores and

https://doi.org/10.1016/j.heliyon.2018.e00654

released free Br- anions. Therefore, phase (2) is assigned to $TaBr_xO_y$ compound, yielding due to the decomposition of $\{Ta_6Br_{12}\}$ species.

Both the phase (3) and (4) refer to the nonembedded tantalum compounds, whereas they showed distinct texture in HAADF-STEM observation and possibly relate to different forming mechanism. The tantalum compounds in phase (3) can also be assigned to the discrete $\{Ta_6Br_{12}\}$ species, as they show comparable size with those in phase (1). Further TEM observations (Fig. 13) indicated the affinity of those compounds with the surfactants Brij L4 on the out surface of SiO_2 nanoparticles. Therefore, phase (3) were possibly originated by the coordination of $\{Ta_6Br_{12}\}$ species with the -OH groups of the Brij L4. Since these complexes in RM system stay between oil and aqueous phase, that this part of $\{Ta_6Br_{12}\}$ species were not embedded into SiO_2 matrix but immobilized on its out surface. Indeed, phase (3) disappeared along with the removing of surfactants within washing steps. On contrary, the tantalum compounds in phase (4) show an irregular shape and much larger size—even larger than the size of SiO_2 nanoparticles under some certain synthetic conditions. The ICP-OES/IC analysis suggested that the presence of phase (4) closely relates with the saturation of tantalum compounds in SiO_2 matrix. In this study, we observed such saturation occurred when C_{TBH} reached 30 mM, and a higher C_{TBH} did not increase the amount of embedded tantalum compounds but resulted in the emerging of phase (4). Therefore, the phase (4) are possibly the promptly generated precipitates $[\{Ta_6Br^i_{12}\}(OH)^a_x(H_2O)^a_{6\text{-}x}]\cdot nH_2O$ (x = 2, 3, 4), whose size was so large that could not entirely stay inside the "nanoreactors" of RM system or further be encapsulated by SiO_2. On another hand, the molar ratio of ethanol: H_2O (R) in the RM system also acted as an important parameter, as the phase (4) promptly generated when

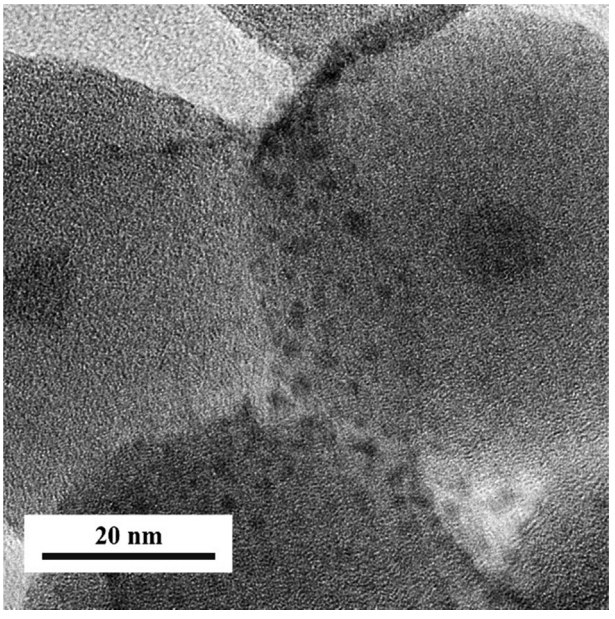

Fig. 13. TEM image of the $\{Ta_6Br_{12}\}@SiO_2$ nanoparticles sampled before washing steps.

https://doi.org/10.1016/j.heliyon.2018.e00654

both C_{TBH} and R was low. This phenomenon can be explained by the different behavior of $[\{Ta_6Br^i_{12}\}(H_2O)^a_6]^{2+}$ cluster units in water and water-ethanol mixture. Indeed, the precipitates $[\{Ta_6Br^i_{12}\}(OH)^a_x(H_2O)^a_{6-x}]\cdot nH_2O$ can be re-dissolved by alkoxides, rendering more discrete $\{Ta_6Br_{12}\}$ species staying in basic solution [45].

5. Conclusion

In this study, we successfully embedded discrete hexanuclear tantalum bromide cluster units $[\{Ta_6Br^i_{12}\}L^a_6]$ (i = inner, a = apical, L = ligand OH or H_2O) inside SiO_2 nanoparticles by a reverse microemulsion (RM) based synthesis for the first time. The compound $[\{Ta_6Br^i_{12}\}Br^a_2(H_2O)^a_4]\cdot nH_2O$ (TBH) was used as the starting material and the RM system was composed by n-heptane, Brij L4, ethanol, ammonia solution and the TBH sol. Thanks to the well confined water phase in RM system, the obtained $\{Ta_6Br_{12}\}@SiO_2$ nanoparticles showed narrow size distribution and averages size of 40−50 nm. The presence of discrete $\{Ta_6Br_{12}\}$ species inside SiO_2 matrix was confirmed by HAADF-STEM and EDS mapping analyses, and XPS characterization further demonstrated their integrity. However, a series of ICP-OES/IC characterizations revealed not all the embedded tantalum compounds were discrete $\{Ta_6Br_{12}\}$ species, as a $TaBr_xO_y$ particle with the size ca. 10 nm was found as the core in each SiO_2 nanoparticles. Formation of this kind of by-products was possibly due to the decomposition of Ta_6Br_{12} structural edifice in the presence of NH_4OH. Other kind of by-products (*i.e.*, nonembedded tantalum compounds) could be removed in post-treatments or be prevented their generation by adjusting synthetic parameters. The diffuse reflectance UV-vis spectrum not only indicated the presence of discrete $\{Ta_6Br_{12}\}$ species in SiO_2 nanoparticles but also further revealed that 3+ is their stable oxidation state. Indeed, the embedded discrete $\{Ta_6Br_{12}\}$ species maintained the optical properties of those in solution—showing strong absorptions in both UV and NIR region. Therefore, the $\{Ta_6Br_{12}\}@SiO_2$ nanoparticles we synthesized in this study are promising for the filtration of the most energetic UV-NIR radiations or biotechnology applications. More generally, this work paves the way to the preparation of inorganic nanocomposites powders based on Ta_6 metal clusters.

Declarations

Author contribution statement

Wanghui Chen: Conceived and designed the experiments; Performed the experiments; Analyzed and interpreted the data; Contributed reagents, materials, analysis tools or data; Wrote the paper.

Fabien Grasset: Conceived and designed the experiments; Contributed reagents, materials, analysis tools or data.

https://doi.org/10.1016/j.heliyon.2018.e00654

Maxence Wilmet, Thai Giang Truong, Noée Dumait, Stéphane Cordier, Yoshio Matsui, Toru Hara, Toshiaki Takei, Norio Saito, Thi Kim Ngan Nguyen, Takeo Ohsawa, Naoki Ohashi, Tetsuo Uchikoshi: Contributed reagents, materials, analysis tools or data.

Funding statement

This work was supported by Saint-Gobain (France), CNRS, Université de Rennes 1, and NIMS through the Laboratory for Innovative Key Materials and Structures (LINK UMI 3629).

Competing interest statement

The authors declare no conflict of interest.

Additional information

No additional information is available for this paper.

Acknowledgements

This work was carried out as part of the France-Japan international collaboration framework (UMI 3629-LINK Center). The authors wish to thank the people involved in LINK and related activities, particularly David Lechevalier and Dr. Mari Kono of Saint-Gobain KK (Tokyo, Japan).

References

[1] J. Lowe, D. Stock, B. Jap, P. Zwickl, W. Baumeister, R. Huber, Crystal structure of the 20S proteasome from the archaeon T. acidophilum at 3.4 A resolution, Science 268 (1995) 533−539.

[2] P. Cramer, D.A. Bushnell, J. Fu, A.L. Gnatt, B. Maier-Davis, N.E. Thompson, R.R. Burgess, A.M. Edwards, P.R. David, R.D. Kornberg, Architecture of RNA polymerase II and implications for the transcription mechanism, Science 288 (2000) 640−649.

[3] K.N. Ferreira, T.M. Iverson, K. Maghlaoui, J. Barber, Architecture of the photosynthetic oxygen-evolving center, Science 43 (2004) 1831−1839.

[4] B.F. Mullan, M.T. Madsen, L. Messerle, V. Kolesnichenko, J. Kruger, X-ray attenuation coefficients of high-atomic-number, hexanuclear transition metal cluster compounds: a new paradigm for radiographic contrast agents, Acad. Radiol. 7 (2000) 254−259.

https://doi.org/10.1016/j.heliyon.2018.e00654

[5] A. Renaud, M. Wilmet, T.G. Truong, M. Seze, P. Lemoine, N. Dumait, W. Chen, N. Saito, T. Ohsawa, T. Uchikoshi, N. Ohashi, S. Cordier, F. Grasset, Transparent tantalum cluster-based UV and IR blocking electrochromic devices, J. Mater. Chem. C 5 (2017) 8160−8168.

[6] N.T. Nguyen, A. Renaud, M. Wilmet, N. Dumait, S. Paofai, D. Benjamin, W. Chen, N. Ohashi, S. Cordier, F. Grasset, T. Uchikoshi, New ultra-violet and near-infrared blocking filters for saving energy applications: fabrication of tantalum metal atom cluster-based nanocomposite thin films by electrophoretic deposition, J. Mater. Chem. C 5 (2017) 10477−10484.

[7] E.J. Welch, J.R. Long, Atomlike Building Units of Adjustable Character: Solid-state and Solution Routes to Manipulating Hexanuclear Transition Metal Chalcohalide Clusters, John Wiley & Sons, NJ, 2005.

[8] B. Perić, D. Jozić, P. Planinić, N. Brničević, G. Giester, Synthesis, crystal structure, spectroscopic and thermal properties of $[Et_4N][Ta_6Br_{12}(H_2O)_6]Br_4\cdot 4H_2O$ (Et=ethyl)-a new compound with the paramagnetic $[Ta_6Br_{12}]^{3+}$ cluster core, J. Solid State Chem. 182 (2009) 2443−2450.

[9] F. Ogliaro, S. Cordier, J.-F. Halet, C. Perrin, J.-Y. Saillard, M. Sergent, Detailed structural and theoretical studies of the bonding in edge-bridged halide and oxyhalide octahedral niobium and tantalum clusters, Inorg. Chem. 37 (1998) 6199−6207.

[10] T.G. Gray, Hexanuclear and higher nuclearity clusters of the groups 4-7 metals with stabilizing π-donor ligands, Coord. Chem. Rev. 243 (2003) 213−235.

[11] D. Bauer, H.-G. Schnering, Beiträge zur Chemie der Elemente Niob und Tantal. LXVII. Die Struktur der Tantalhalogenide Ta_6Cl_{15} und Ta_6Br_{15}, Z. Anorg. Allg. Chem. 361 (1968) 259−276.

[12] F.W. Koknat, J.A. Parsons, A. Vongvusharintra, Metal cluster halide complexes. i. efficient synthesis of hydrated hexanuclear niobium and tantalum cluster halides $M_6X_{14}\cdot 8H_2O$, Inorg. Chem. 13 (1974) 1699−1702.

[13] D.N.T. Hay, L. Messerle, Low-temperature, high yield synthesis, and convenient isolation of the high-electron-density cluster compound Ta_6Br_{14} $8H_2O$ for use in biomacromolecular crystallographic phase determination, J. Struct. Biol. 139 (2002) 147−151.

[14] B.G. Hughes, J.L. Meyer, P.B. Fleming, R.E. Mccarley, Chemistry of polynuclear metal halides. III. synthesis of some niobium and tantalum $m_6x_{12}^{n+}$ cluster derivatives, Inorg. Chem. 9 (1970) 1343−1346.

https://doi.org/10.1016/j.heliyon.2018.e00654

[15] P.A. Vaughan, J.H. Sturdivant, L. Pauling, The determination of the structures of complex molecules and ions from X-ray diffraction by their solutions: the structures of the groups $PtBr_6^{-}$, $PtCl_6^{-}$, $Nb_6Cl_{12}^{++}$, $Ta_6Br_{12}^{++}$, and $Ta_6Cl_{12}^{++}$, J. Am. Chem. Soc. 72 (1950) 5477−5486.

[16] N. Prokopuk, D.F. Shriver, The octahedral M_6Y_8 and M_6Y_{12} clusters of group 4 and 5 transition metals, Adv. Inorg. Chem. 46 (1998) 1−49.

[17] Š.M.N. Brničević, Cluster hydroxides of the composition $M_2[Ta_6Cl_{12}](OH)_6$ nH_2O with M=Na, K, Rb, $(CH_3)_4N^+$ and $(C_2H_5)_4N^+$ air oxidation of the cluster unit $[Ta_6Cl_{12}]^{2+}$ in alkaline medium, Croat. Chem. Acta 57 (1984) 529−535.

[18] A. Kashta, N. Brničeaić, R.E. Mccarley, Reactions of niobium and tantalum clusters with aliphatic alcohols. Synthesis and properties of $[M_6X_{12}(ROH)_6]$ X_2, M = Nb or Ta, X = Cl or Br, R = Me, Et, i-Pr or i-Bu, Polyhedron 10 (1991) 2031−2036.

[19] M.N. Sokolov, P.A. Abramov, M.A. Mikhailov, E.V. Peresypkina, A.V. Virovets, V.P. Fedin, Simplified synthesis and structural study of $\{Ta_6Br_{12}\}$ clusters, Z. Anorg. Allg. Chem. 636 (2010) 1543−1548.

[20] M.B. Robin, N.A. Kuebler, Color and nonintegral valence in niobium and tantalum subhalides, Inorg. Chem. 4 (1965) 978−985.

[21] B. Spreckelmeyer, Absorptionsspektren von verbindungen mit $[Nb_6X_{12}]$- und $[Ta_6X_{12}]$-gruppen (X = Halogen), Z. Anorg. Allg. Chem. 365 (1969) 225−242.

[22] P.B. Fleming, J.L. Meyer, W.K. Grindstaff, R.E. McCarley, Chemistry of polynuclear metal halides. VIII. Infrared spectra of some $Nb_6X_{12}^{n+}$ and $Ta_6X_{12}^{n+}$ derivatives, Inorg. Chem. 9 (1970) 1769−1771.

[23] K. Osseo-Asare, F.J. Arriagada, Preparation of SiO_2 nanoparticles in a non-ionic reverse micellar system, Colloids Surf 50 (1990) 321−339.

[24] C.-L. Chang, H.S. Fogler, Kinetics of silica particle formation in nonionic W/O microemulsions from TEOS, Mater. Interfaces Electrochem. Phenom. 42 (1996) 3153−3163.

[25] K.S. Finnie, J.R. Bartlett, C.J.A. Barbé, L. Kong, Formation of silica nanoparticles in microemulsions, Langmuir 23 (2007) 3017−3024.

[26] S.Y. Chang, L. Liu, S.A. Asher, Preparation and properties of tailored morphology, monodisperse colloidal silica-cadmium sulfide nanocomposites, J. Am. Chem. Soc. 116 (1994) 6739−6744.

https://doi.org/10.1016/j.heliyon.2018.e00654

[27] T. Aubert, F. Grasset, S. Mornet, E. Duguet, O. Cador, S. Cordier, Y. Molard, V. Demange, M. Mortier, H. Haneda, Functional silica nanoparticles synthesized by water-in-oil microemulsion processes, J. Colloid Interface Sci. 341 (2010) 201−208.

[28] A. Guerrero-Martínez, J. Pérez-Juste, L.M. Liz-Marzán, Recent progress on silica coating of nanoparticles and related nanomaterials, Adv. Mater. 22 (2010) 1182−1195.

[29] J. Wang, Z.H. Shah, S. Zhang, R. Lu, Silica-based nanocomposites via reverse microemulsions: classifications, preparations, and applications, Nanoscale 6 (2014) 4418.

[30] A.K. Ganguli, T. Ahmad, S. Vaidya, J. Ahmed, Microemulsion route to the synthesis of nanoparticles, Pure Appl. Chem. 80 (2008) 2451−2477.

[31] T. Ahmad, A.K. Ganguli, Structural and dielectric characterization of nanocrystalline (Ba, Pb)ZrO_3 developed by reverse micellar synthesis, J. Am. Ceram. Soc. 89 (2006) 3140−3146.

[32] T. Ahmad, K. Ramanujachary, S.E. Lofland, A.K. Ganguli, Reverse micellar synthesis and properties of nanocrystalline GMR materials ($LaMnO_3$, $La_{0·67}Sr_{0·33}$ MnO_3 and $La_{0·67}$ $Ca_{0·33}$ MnO_3): ramifications of size, J. Chem. Sci. 118 (2006) 513−518.

[33] R. Koole, M.M. Van Schooneveld, J. Hilhorst, C.D.M. Donegá, C. Hart, A. Van Blaaderen, D. Vanmaekelbergh, A. Meijerink, D.C. Hart, On the incorporation mechanism of hydrophobic quantum dots in silica spheres by a reverse microemulsion method on the incorporation mechanism of hydrophobic quantum dots in silica spheres by a reverse microemulsion method, Chem. Mater. 20 (2008) 2503−2512.

[34] Y. Zhu, F.Y. Jiang, K. Chen, F. Kang, Z.K. Tang, Modified reverse microemulsion synthesis for iron oxide/silica core-shell colloidal particles, J. Sol. Gel Sci. Technol. 66 (2013) 180−186.

[35] F. Grasset, N. Labhsetwar, D. Li, D.C. Park, N. Saito, H. Haneda, O. Cador, T. Roisnel, S. Mornet, E. Duguet, J. Portier, J. Etourneau, Synthesis and magnetic characterization of zinc ferrite nanoparticles with different environments: powder, colloidal solution, and zinc ferrite-silica core-shell nanoparticles, Langmuir 18 (2002) 8209−8216.

[36] F. Grasset, R. Marchand, A.M. Marie, D. Fauchadour, F. Fajardie, Synthesis of CeO_2@SiO_2 core-shell nanoparticles by water-in-oil microemulsion. Preparation of functional thin film, J. Colloid Interface Sci. 299 (2006) 726−732.

 https://doi.org/10.1016/j.heliyon.2018.e00654

[37] J.H. Son, H.Y. Park, D.P. Kang, D.S. Bae, Synthesis and characterization of Ag/Pd doped SiO_2 nanoparticles by a reverse micelle and sol-gel processing, Colloids Surf. A 313−314 (2008) 105−107.

[38] J. Qian, Z. Zhou, X. Cao, S. Liu Songqin, Electrochemiluminescence immunosensor for ultrasensitive detection of biomarker using $Ru(bpy)_3^{2+}$-encapsulated silica nanosphere labels, Anal. Chim. Acta 665 (2010) 32−38.

[39] H.L. Ding, Y.X. Zhang, S. Wang, J.M. Xu, S.C. Xu, G.H. Li, Fe_3O_4@SiO_2 core/shell nanoparticles: the silica coating regulations with a single core for different core sizes and shell thicknesses, Chem. Mater. 24 (2012) 4572−4580.

[40] F. Grasset, F. Dorson, S. Cordier, Y. Molard, C. Perrin, A.-M. Marie, T. Sasaki, H. Haneda, Y. Bando, M. Mortier, Water-in-oil microemulsion preparation and characterization of $Cs_2[Mo_6X_{14}]$@SiO_2 phosphor nanoparticles based on transition metal clusters (X = Cl, Br, and I), Adv. Mater. 20 (2008) 143−148.

[41] T. Aubert, F. Cabello-Hurtado, M.A. Esnault, C. Neaime, D. Lebret-Chauvel, S. Jeanne, P. Pellen, C. Roiland, L. Le Polles, N. Saito, K. Kimoto, H. Haneda, N. Ohashi, F. Grasset, S. Cordier, Extended investigations on luminescent $Cs_2[Mo_6Br_{14}]$@SiO_2 nanoparticles: physico-structural characterizations and toxicity studies, J. Phys. Chem. C 117 (2013) 20154−20163.

[42] Y.A. Vorotnikov, O.A. Efremova, N.A. Vorotnikova, K.A. Brylev, M.V. Edeleva, A.R. Tsygankova, A.I. Smolentsev, N. Kitamura, Y.V. Mironov, M.A. Shestopalov, On the synthesis and characterisation of luminescent hybrid particles: Mo_6 metal cluster complex/SiO_2, RSC Adv. 6 (2016) 43367−43375.

[43] C. Neaime, M. Amela-Cortes, F. Grasset, Y. Molard, S. Cordier, B. Dierre, M. Mortier, T. Takei, K. Takahashi, H. Haneda, M. Verelst, S. Lechevallier, Time-gated luminescence bioimaging with new luminescent nanocolloids based on $[Mo_6I_8(C_2F_5COO)_6]^{2-}$ metal atom clusters, Phys. Chem. Chem. Phys. 18 (2016) 30166−30173.

[44] A.O. Solovieva, Y.A. Vorotnikov, K.E. Trifonova, O.A. Efremova, A.A. Krasilnikova, K.A. Brylev, E.V. Vorontsova, P.A. Avrorov, L.V. Shestopalova, A.F. Poveshchenko, Y.V. Mironov, M.A. Shestopalov, Cellular internalisation, bioimaging and dark and photodynamic cytotoxicity of silica nanoparticles doped by $\{Mo_6I_8\}^{4+}$ metal clusters, J. Mater. Chem. B 4 (2016) 4839−4846.

https://doi.org/10.1016/j.heliyon.2018.e00654

[45] N. Brničević, H. Schüfer, Die reaktion der komplexe [$M_6X_{12}]X_2$ $8H_2O$ (M = Nb, Ta; X = CI, Br) mit natronlauge, Z. Anorg. Allg. Chem. 441 (1978) 219−229.

[46] P.J. Kuhn, R.E. Mccarley, Chemistry of polynuclear metal halides. I. preparation of the polynuclear tantalum halides Ta_6X_{14}, Inorg. Chem. 4 (1965) 1482−1486.

[47] B. Spreckelmeyer, Beiträge zur chemie der elemente niob und tantal. LXVI. wasserhaltige verbindungen mit [Me_6X_{12}]-gruppen (Me = Nb, Ta; X = Cl, Br), Z. Anorg. Allg. Chem. 358 (1968) 147−162.

[48] S.A. Best, R.A. Walton, X-ray photoelectron spectra of inorganic molecules. 22. Halogen core electron binding energies of low oxidation state molybdenum bromide and molybdenum iodide clusters and niobium and tantalum chlorides containing the $[M_6Cl_{12}]^{n+}$ cores, Inorg. Chem. 18 (1979) 484−488.

[49] B. Spreckelmeyer, H. Schäfer, Die photometrische titration des $[Ta_6Br_{12}]^{2+}$-Ions, J. Less Common Met. 13 (1967) 127−129.

 https://doi.org/10.1016/j.heliyon.2018.e00654